# First-principles simulations and shock Hugoniot calculations of warm dense neon

K. P. Driver[1,*] and B. Militzer[1,2]

[1]*Department of Earth and Planetary Science, University of California, Berkeley, California 94720, USA*
[2]*Department of Astronomy, University of California, Berkeley, California 94720, USA*

All-electron path integral Monte Carlo (PIMC) and density functional theory molecular dynamics (DFT-MD) simulations provide a consistent, first-principles investigation of warm dense neon plasmas in the density-temperature range of 1–15 g cm$^{-3}$ and $10^4$–$10^9$ K. At high temperatures, DFT-MD becomes intractable because of too many partially occupied bands, while at lower temperatures, PIMC is intractable because of the free-particle approximation of fermion nodes. In combination, PIMC and DFT-MD pressures and internal energies provide a coherent equation of state with a region of overlap in which the two methods cross-validate each other. Pair-correlation functions at various temperatures and densities provide details of the plasma structure and the temperature-driven ionization process. The electronic density of states of neon shows that a gap persists for the highest density-temperature conditions studied here with DFT-MD. Finally, the computed shock Hugoniot curves show an increase in compression as the first and second shells are ionized.

## I. INTRODUCTION

Theoretical prediction of thermodynamic properties of warm dense matter [1] (WDM) plays an important role in furthering our understanding of a large variety of high energy density physics applications, including inertial confined plasmas [2,3], shock [4], astrophysical processes [5,6], stellar and planetary interiors [7,8], and supernovae [9]. In order to understand the thermodynamic properties of these physical processes, one must develop accurate methods to predict the equation of state (EOS) of plasmas. The development of a comprehensive first-principles methodology for this purpose remains a great challenge.

The difficulty in treating the physics of the WDM regime is that plasmas are partially ionized such that the electron-ion Coulomb interaction is comparable in magnitude to the kinetic energy. Effects of bonding, ionization, exchange-correlation, and quantum degeneracy all contribute significantly to the total energy [1]. A number of analytic and numerical methods, employing various levels of classical and quantum physics, have been developed to study plasmas in various regimes [10,11], but it is difficult to link them together in a thermodynamically consistent way.

In an effort to develop a comprehensive first-principles treatment of WDM, we have been working on the development of a combined approach using density functional theory molecular dynamics (DFT-MD) at low temperatures and path-integral Monte Carlo (PIMC) at high temperatures [12,13]. Prior to our work, PIMC had been applied only to the lightest two elements, hydrogen [14–16] and helium [12]. We showed that all-electron PIMC with free-particle nodes is a feasible route to study even heavier elements, computing EOSs for both water and carbon plasmas [13,17]. In the work presented here, we aim to press the limits of our technique and show that it is capable of producing an EOS for elements as heavy as neon.

Neon is itself an interesting and important material in the universe, as it is the fifth most abundant element after H, He, O, and C. During nucleosynthesis, neon is created during the carbon-burning process. As an inert, noble gas, neon is highly volatile and, therefore, easily depleted from atmospheres of even giant gas planets such as Jupiter [18]. Due to stellar and planetary interest in neon, a number of studies have been done for various warm and dense conditions [19–21].

In this paper, we aim to produce a comprehensive, first-principles EOS for neon that covers a large range of temperature-density space (0.8949–15.0255 g cm$^{-3}$ and $10^4$–$10^9$ K). In Sec. II, we discuss the details of the PIMC and DFT-MD methods used for our calculations. In Sec. III, we provide the EOS over a wide temperature-density range and show that both PIMC and DFT-MD agree near $1 \times 10^6$ K, where both methods are feasible. In Sec. IV, we characterize the structure of the plasma by looking at various pair-correlation functions of electrons and nuclei as a function of temperature and density. In Sec. V, we discuss the electronic density of states at the most extreme conditions computed here with DFT-MD. We find that a gap persists at $1 \times 10^6$ K and 15.0255 g cm$^{-3}$. Finally, in Sec. VI, we discuss predictions for the shock Hugoniot curves.

## II. METHODS

A rigorous discussion of PIMC [22] and DFT-MD [23] methods and the details of our specific PIMC implementation [12] have been reported previously. In this section, we focus only on details that are important for our neon simulations.

PIMC is a first-principles method for studying materials at high temperature where properties of materials are dominated by excited states. The thermal density matrix, which is efficiently computed within Feynman's path integral formalism, is the natural operator to use for computing high-temperature observables. The PIMC method stochastically solves the full, finite-temperature quantum many-body problem by treating electrons and nuclei on an equal footing. In contrast to DFT-MD, PIMC efficiency increases with temperature as particles

*kdriver@berkeley.edu; http://militzer.berkeley.edu/~driver/

become more classical and fewer time slices are needed to describe quantum mechanical many-body correlations, scaling inversely with temperature.

PIMC uses a fixed nodal surface to avoid the fermion sign problem. Thus far, all PIMC implementations have employed a free-particle nodal structure, which is expected to be a sensible approximation for systems that are close to a fully ionized state. However, reliable results at surprisingly low temperatures have been obtained for hydrogen [14], as well as carbon and water [13]. These results showed that free-particle nodes are sufficient for systems with a filled $1s$ state and $2s$ states that are partially ionized.

For our PIMC simulations, the Coulomb interaction is incorporated via pair density matrices derived from the eigenstates of the two-body Coulomb problem. A sufficiently small time step is determined by converging total energy as a function of time step until the energy changes less than 0.8% (see Supplemental Material [24]). We use a time step of $1/256$ Ha$^{-1}$ for temperatures below $4 \times 10^6$ K and, for higher temperatures, the time step decreases as $1/T$ while keeping at least five time slices in the path integral. In order to minimize finite-size errors, the total energy is converged to better than 0.4% when comparing 8- and 24-atom simple cubic simulation cells (see Supplemental Material [24]).

The framework of DFT provides an exact mapping of the many-body problem onto a single-particle problem, assuming an approximate exchange-correlation (XC) functional is known. For all but the simplest model systems, the most commonly used XC functionals have been constructed from data based on zero-temperature quantum Monte Carlo calculations of the electron gas [25]. In the WDM regime, where temperatures are at or above the Fermi temperature, there is no expectation for an XC functional to provide an accurate description of the electronic physics [26]. However, in previous PIMC and DFT-MD work on helium [12], carbon [13], and water [13], it was shown that DFT functionals are surprisingly accurate at high temperatures.

Finite-temperature DFT uses a Fermi-Dirac function to allow for thermal occupation of single-particle electronic states [27], but requires an increasing number of bands with temperature, crippling its efficiency at extreme temperatures. In addition, typically pseudopotentials replace the core electrons in each atom. It is possible that the pseudopotential approximation may break down and should be compared with all-electron calculations, particularly as electrons are thermally excited out of the core. Orbital-free density functional methods aim to overcome such thermal band limitations, but several challenges remain to be solved [28].

The DFT-MD simulations were performed with the Vienna *Ab initio* Simulation Package (VASP) [29] using the projector augmented-wave (PAW) method [30]. MD uses an *NVT* ensemble regulated with a Nosé-Hoover thermostat. Exchange-correlation effects are described using the Perdew-Burke-Ernzerhof [31] generalized gradient approximation. Electronic wave functions are expanded in a plane-wave basis with a energy cutoff of at least 1000 eV in order to converge total energy to chemical accuracy. Size convergence tests up to a 24-atom simulation cell at temperatures of 10 000 K and above indicate that total energies are converged to better than 0.1% in a 24-atom simple cubic cell (see Supplemental

Material [24]). We find, at temperatures above 250 000 K, 8-atom cell results are sufficient since the kinetic energy far outweighs the interaction energy at such high temperatures. The number of bands in each calculation is selected such that thermal occupation is converged to better than $10^{-4}$, which requires up to 9000 bands in the highest temperature cases corresponding with the lowest density. All simulations are performed at the $\Gamma$ point of the Brillouin zone, which is sufficient for high-temperature fluids, converging total energy to better than 0.01% relative to a comparison with a grid of $k$ points.

## III. EQUATION OF STATE RESULTS

In this section, we report our EOS results for four densities of 0.8949, 3.7283, 7.8959, and 15.0255 g cm$^{-3}$ and for a temperature range of $10^4 - 10^9$ K. The four isochores are shown in Fig. 1, which is discussed in more detail in Sec. VI.

Figure 2 compares pressures obtained for neon from PIMC and DFT-MD simulations and from the analytical Debye-Hückel plasma model [32]. Pressures, $P$, are plotted relative to a fully ionized Fermi gas of electrons and ions with pressure, $P_0$, in order to compare only the excess pressure contributions that result from particle interactions. DFT-MD excess pressures agree with PIMC to better than 0.05% at $10^6$ K for the largest three densities. For the lowest density, we were unable to obtain converged DFT result at $10^6$ K, and free-particle nodes in PIMC start to break down at that temperature. Nonetheless, the excellent agreement near $10^6$ K at all higher densities allows for cross-validation between DFT and PIMC, which implies the zero temperature DFT exchange-correlation potential remains valid at high temperatures and that the free-particle nodal approximation is valid in PIMC when atoms are partially and fully ionized. For the smallest density, we find that the $2s$ state is 15% occupied when free-particle nodes start to break down, while for the largest density, the $2s$ state is 50% occupied at the breaking point.
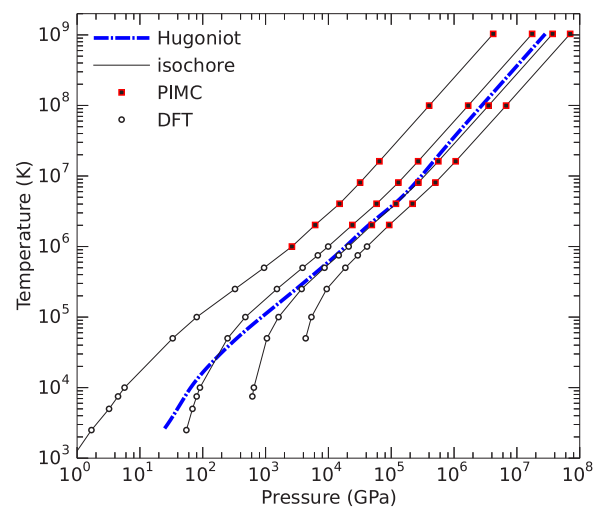


FIG. 1. (Color online) Temperature-pressure conditions for the PIMC and DFT-MD calculations along four isochores corresponding to the densities of 0.8949, 3.7283, 7.8959, and 15.0255 g cm$^{-3}$. The dash-dotted line shows the Hugoniot curve for an initial density of $\rho_0 = 1.5070$ g cm$^{-3}$.
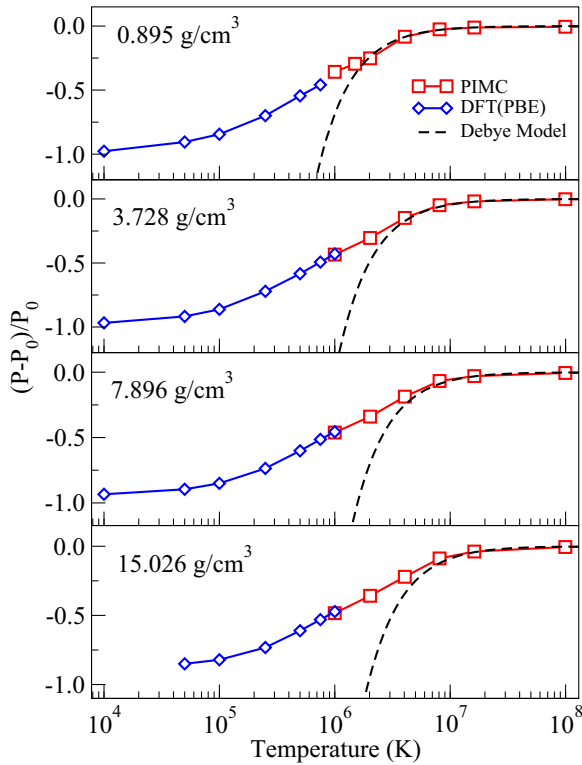
FIG. 2. (Color online) Comparison of excess pressure relative to the ideal Fermi gas plotted as a function of temperature for neon.

The two methods have comparable computational cost in the overlap region, but DFT starts to become prohibitive beyond $7.5 \times 10^5$ K, and free-particle nodes break down below $10^6$ K for all densities.

Figure 3 compares internal energies, $E$, plotted relative to the internal energy of a fully ionized Fermi gas, $E_0$. PIMC and DFT-MD results for excess internal energy agree to better than 0.04% at $10^6$ K for the largest three densities. The DFT-MD and PIMC methods together form a coherent equation of state over all temperatures ranging to the weakly interacting plasma limit. PIMC extends the equations of state to the weakly interacting plasma limit at high temperatures, in agreement with the Debye-Hückel model [32].

Table I provides the densities, temperatures, and the raw pressures and energies used to construct our equations of state. The DFT-MD energies have been shifted by 128.8661280 Ha/atom in order to shift the the PAW pseudopotential reference energy back to the absolute atomic energy. The shift was calculated by performing an all-electron atomic calculation in the OPIUM code [33] and a corresponding isolated-atom calculation in VASP.

The EOS table also allows one to compare the PIMC and DFT-MD internal energies and pressures at $1 \times 10^6$ K, where the two methods provide overlapping EOS data at the highest three densities. There is roughly a 2%–3% discrepancy between the DFT and PIMC raw energies and 1%–2% in the total pressures at that temperature. There are three potential sources of this discrepancy: (1) the use of free-particle nodes in PIMC, (2) employment of the PBE exchange-correlation functional in DFT-MD that was constructed for ground-state calculations, and (3) insufficiency of the VASP DFT-MD
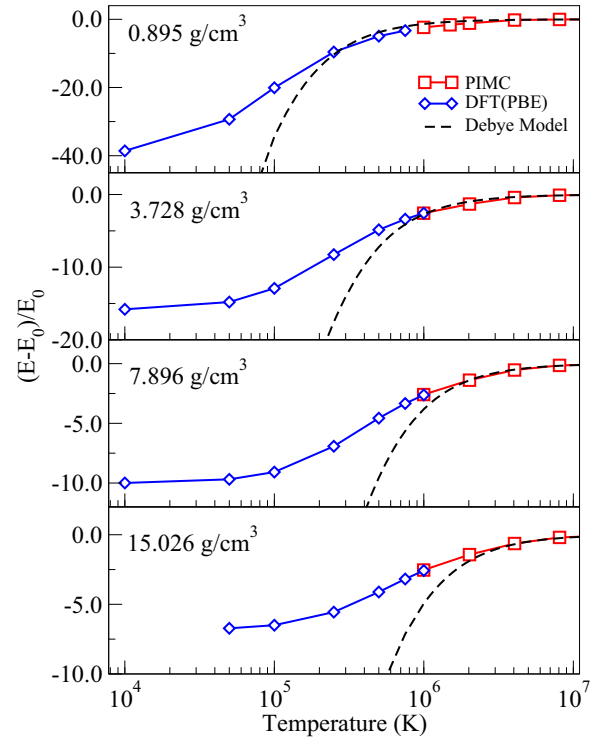


FIG. 3. (Color online) Comparison of excess internal energies relative to the ideal Fermi gas plotted as a function of temperature for neon.

pseudopotential to include effects of core excitations. There is currently no straightforward method to test the size of the error introduced by the PIMC free-particle node approximation and DFT-MD exchange-correlation approximation.

However, the accuracy of the VASP pseudopotential at $1 \times 10^6$ K can be tested by comparing with the results of an all-electron calculation. We constructed a neon pseudopotential (cutoff radius of 0.1 Bohr radii) that includes all electrons in the valence using the fhi98PP code [34]. This pseudopotential can be used for finite temperature DFT calculations in the ABINIT code [35]. We compared the VASP and all-election ABINIT DFT energies for a static calculation of neon at $1 \times 10^6$ K and found that the VASP pseudopotential calculation is 0.73 Ha too low in energy. This means that the unincorporated effects of core excitations in the VASP pseudopotential approximation at $1 \times 10^6$ K account for nearly one-third of the discrepancy we find between the PIMC and DFT-MD internal energies. Therefore, only 1%–2% of the discrepancy between PIMC and DFT is due to the combined effects of the free-particle node approximation in PIMC and the exchange-correlation approximation in DFT-MD.

## IV. PAIR-CORRELATION FUNCTIONS

In this section, we study the structure of neon plasmas. Pair-correlation functions [36] between the various particles are analyzed as a function of temperature and density. The data give insight into details of the temperature-driven ionization process.

Figure 4 shows nuclear pair-correlation functions, $g(r)$, computed with PIMC. At low temperature, the atoms are

TABLE I. EOS table with pressures and internal energies at all temperature and density conditions considered in this work. The numbers in parentheses indicate the statistical uncertainties of the DFT-MD and PIMC simulations.

| $\rho$ (g cm$^{-3}$) | $T$ (K) | $P$ (GPa) | $E$ (Ha/atom) |
|---|---|---|---|
| 0.8948[a] | 1034730000 | 4196329(484) | 54055(6) |
| 0.8948[a] | 99497670 | 401383(260) | 5170(3) |
| 0.8948[a] | 16167700 | 64842(37) | 826.1(5) |
| 0.8948[a] | 8083850 | 31972(14) | 400.5(3) |
| 0.8948[a] | 4041920 | 15045(7) | 164.5(2) |
| 0.8948[a] | 2020960 | 6150(18) | −15.7(3) |
| 0.8948[a] | 1497010 | 4305(13) | −49.0(2) |
| 0.8948[a] | 998004 | 2625(25) | −72.2(3) |
| 0.8948[b] | 750000 | 1666.9(1) | −91.746(1) |
| 0.8948[b] | 500000 | 946.5(1) | −105.992(1) |
| 0.8948[b] | 250000 | 326.1(4) | −120.226(1) |
| 0.8948[b] | 100000 | 80.1(2) | −126.792(1) |
| 0.8948[b] | 50000 | 33.2(8) | −128.204(1) |
| 0.8948[b] | 10000 | 5.70(5) | −128.816(1) |
| 0.8948[b] | 7500 | 4.48(4) | −128.829(1) |
| 0.8948[b] | 5000 | 3.23(2) | −128.842(1) |
| 0.8948[b] | 2500 | 1.69(2) | −128.856(1) |
| 0.8948[b] | 1000 | 0.83(2) | −128.864(1) |
| 3.7283[a] | 1034730000 | 17481714(2218) | 54050(7) |
| 3.7283[a] | 99497670 | 1678235(1064) | 5181(3) |
| 3.7283[a] | 16167700 | 268122(157) | 813.3(5) |
| 3.7283[a] | 8083850 | 130114(63) | 379.5(3) |
| 3.7283[a] | 4041920 | 58450(28) | 123.7(1) |
| 3.7283[a] | 2020960 | 24061(78) | −33.0(2) |
| 3.7283[a] | 998004 | 9895(20) | −84.82(8) |
| 3.7283[b] | 1000000 | 9991(4) | −86.757(6) |
| 3.7283[b] | 750000 | 6786(4) | −99.176(7) |
| 3.7283[b] | 500000 | 3882(4) | −111.229(5) |
| 3.7283[b] | 250000 | 1516(4) | −122.180(6) |
| 3.7283[b] | 100000 | 477(2) | −127.211(4) |
| 3.7283[b] | 50000 | 248(4) | −128.280(5) |
| 3.7283[b] | 10000 | 90.2(2) | −128.767(1) |
| 3.7283[b] | 7500 | 80.0(2) | −128.786(1) |
| 3.7283[b] | 5000 | 68.6(1) | −128.804(1) |
| 3.7283[b] | 2500 | 54.9(1) | −128.825(1) |
| 7.8959[a] | 1034730000 | 37020409(4549) | 54042(7) |
| 7.8959[a] | 99497670 | 3540121(2430) | 5155(4) |
| 7.8959[a] | 16167700 | 561943(312) | 798.5(5) |
| 7.8959[a] | 8083850 | 270886(130) | 362.6(3) |
| 7.8959[a] | 4041920 | 118753(49) | 99.5(1) |
| 7.8959[a] | 2020960 | 49057(164) | −41.8(2) |
| 7.8959[a] | 998004 | 20730(46) | −89.15(7) |
| 7.8959[b] | 1000000 | 21007(24) | −91.25(2) |
| 7.8959[b] | 750000 | 14588(36) | −102.47(2) |
| 7.8959[b] | 500000 | 8675(37) | −113.23(1) |
| 7.8959[b] | 250000 | 3750(18) | −122.78(1) |
| 7.8959[b] | 100000 | 1608(9) | −127.125(7) |
| 7.8959[b] | 50000 | 1050(8) | −128.105(6) |
| 7.8959[b] | 10000 | 650.8(5) | −128.576(1) |
| 7.8959[b] | 7500 | 616.1(7) | −128.576(1) |
| 15.0255[a] | 1034730000 | 70454931(8274) | 54044(6) |
| 15.0255[a] | 99497670 | 6738033(4770) | 5152(4) |
| 15.0255[a] | 16167700 | 1061043(1255) | 785(1) |
| 15.0255[a] | 8083850 | 505320(302) | 342.8(3) |
| 15.0255[a] | 4041920 | 218379(136) | 79.1(1) |

TABLE I. (*Continued.*)

| $\rho$ (g cm$^{-3}$) | $T$ (K) | $P$ (GPa) | $E$ (Ha/atom) |
|---|---|---|---|
| 15.0255[a] | 2020960 | 92899(342) | −47.6(2) |
| 15.0255[a] | 998004 | 40246(83) | −91.88(7) |
| 15.0255[b] | 1000000 | 41119(26) | −94.37(1) |
| 15.0255[b] | 750000 | 29324(37) | −104.66(2) |
| 15.0255[b] | 500000 | 18607(35) | −114.22(1) |
| 15.0255[b] | 250000 | 9400(17) | −122.70(1) |
| 15.0255[b] | 100000 | 5370(23) | −126.55(1) |
| 15.0255[b] | 50000 | 4346(20) | −127.44(1) |

[a]PIMC.
[b]DFT-MD.

kept farthest apart as atoms are repelled by Pauli repulsion among the bound electrons as well as by their Coulomb interaction. As temperature increases, the nuclei gain kinetic energy leading to stronger collisions, and atoms become more ionized, gradually minimizing effects of Pauli repulsion. At the highest temperature, the system approaches the Debye-Hückel limit, behaving like a correlated system of screened Coulomb charges. The $g(r)$ functions depend only weakly on the density. Still, at high density, the chance of finding two nuclei at close range is slightly increased.

Figure 5 compares the nuclear pair-correlation functions of PIMC and DFT at a temperature of $1 \times 10^6$ K. These $g(r)$ curves verify that PIMC and DFT predict consistent structural properties in addition to the agreement in the equation of state.

Figure 6 shows $N(r)$, the integral of the pair correlations, which represents the average number of electrons within a
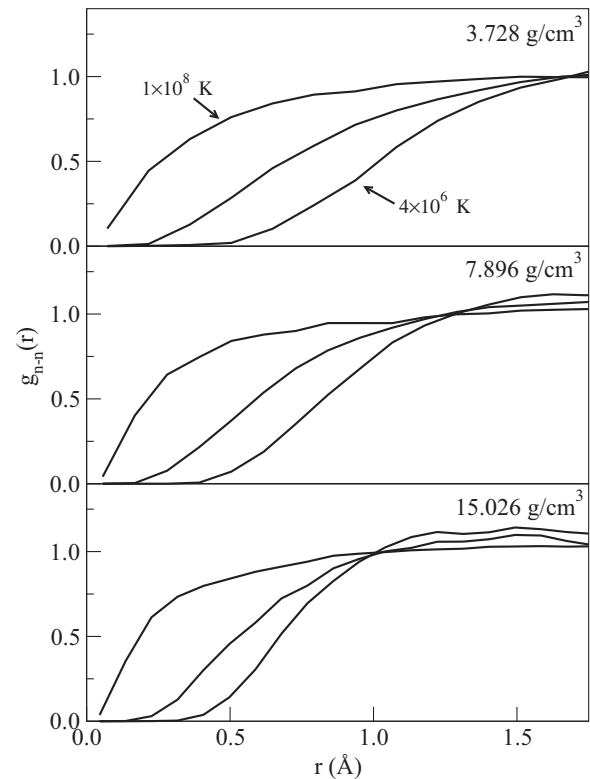


FIG. 4. Nuclear pair-correlation functions for neon from PIMC at temperatures of $4 \times 10^6$, $1.6 \times 10^7$, and $1 \times 10^8$ K for each density.
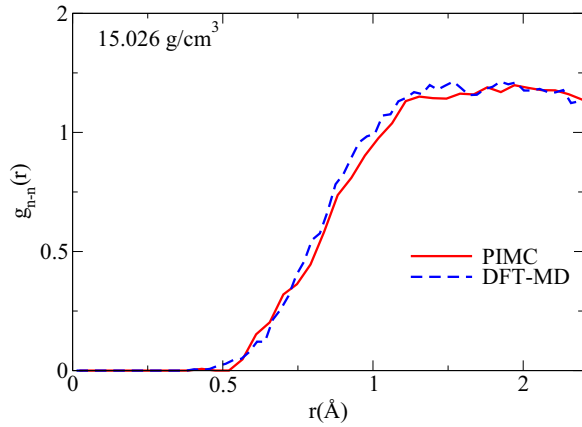
FIG. 5. (Color online) Comparison of PIMC and DFT nuclear pair-correlation functions for neon at $1 \times 10^6$ K.

sphere of radius $r$ around a given nucleus. $N(r)$ decreases with increasing temperature as atoms become ionized and electrons become unbound. At low density, the $1s$ core state is fully occupied at $1 \times 10^6$ K, as it agrees with the isolated $1s$ core state. Ionization of the $1s$ state occurs over the temperature interval from 1 to $8 \times 10^6$ K. At high density, the $1s$ core state is still fully occupied at temperatures up to $2 \times 10^6$ K, indicating that the ionization fraction decreases with density and is not a pressure-driven process as would be expected if neon were close to metallization. In the next section, we will
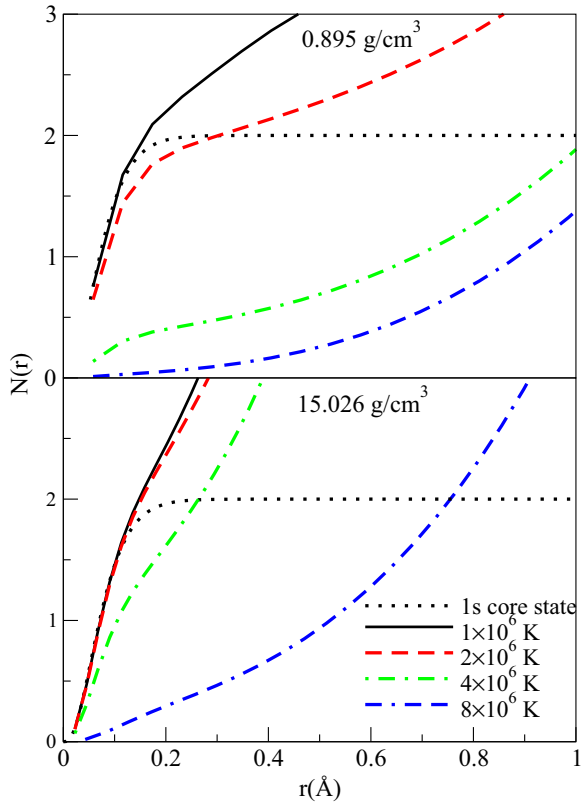


FIG. 6. (Color online) Number of electrons contained in a sphere of radius, $r$, around a neon nucleus. PIMC data at four temperatures are compared with the analytic $1s$ core state.
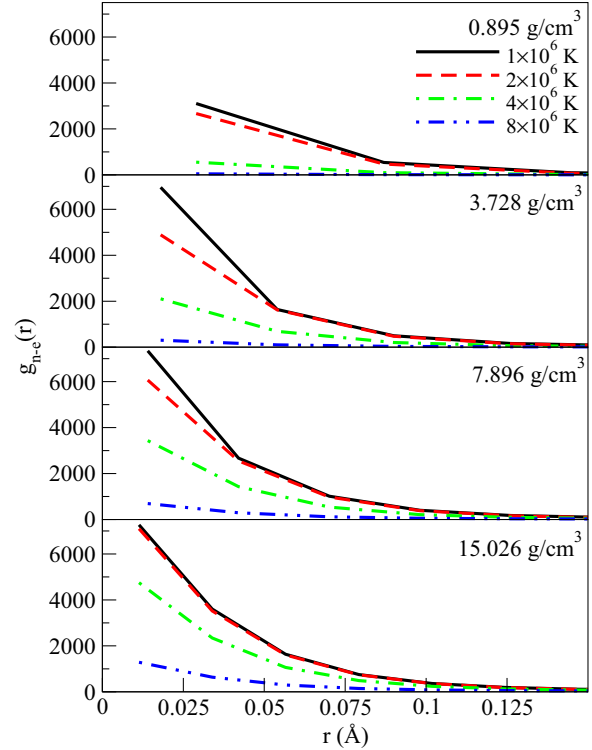


FIG. 7. (Color online) The nucleus-electron pair-correlation functions calculated with PIMC for neon.

further show that neon maintains a gap in its electronic density of states for all densities under consideration.

Figure 7 shows nucleus-electron pair correlations as a function of temperature and density. At low temperature and high density, we find more electrons near the nuclei, reflecting a lower ionization fraction. At higher temperatures, electrons are thermally excited and gradually become unbound, decreasing their correlation with the nuclei. As the density is increased, the electrons are more likely to reside near the nuclei confirming the absence of any pressure-drive ionization as seen in Fig. 6.

Figure 8 shows electron-electron pair correlations with their spins opposite. The function is multiplied by the particle density $\rho$ in units of g cm$^{-3}$, so that the integral under the curves is related to the number of electrons. The electrons are most highly correlated for low temperatures since electrons are most strongly bound to the nuclei in those cases. As temperature increases, electrons are thermally excited, decreasing the correlation. Higher densities increase correlation at short distances, consistent with a lower ionization fraction.

Figure 9 shows electron-electron pair correlations with spins parallel multiplied by the particle density $\rho$. Different electrons with parallel spins are bound to a single nucleus, which leads to a positive correlation at intermediate distances. For short separations, Pauli exclusion takes over and the functions decay to zero for small $r$.

## V. ELECTRONIC DENSITY OF STATES

In this section, we briefly examine whether the effects of high temperature and density can introduce closure of the electronic band gap in fluid neon. Solid neon is the material
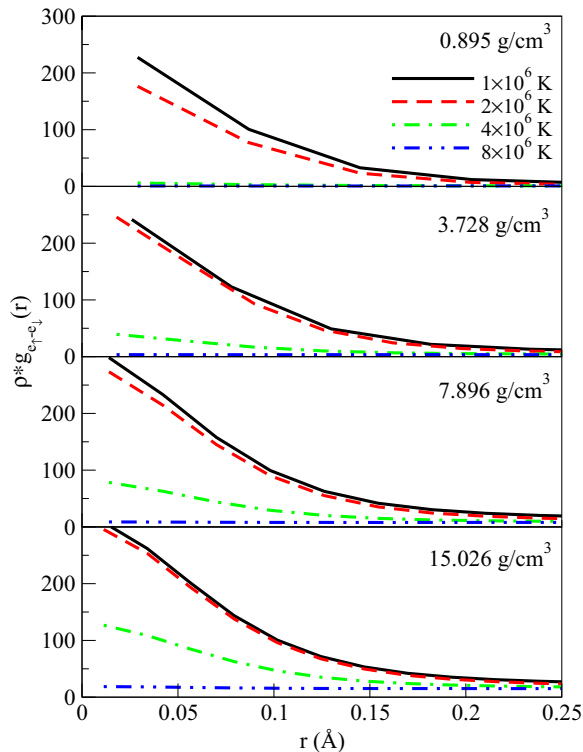
FIG. 8. (Color online) The electron-electron pair-correlation functions for electrons with opposite spins calculated with PIMC.
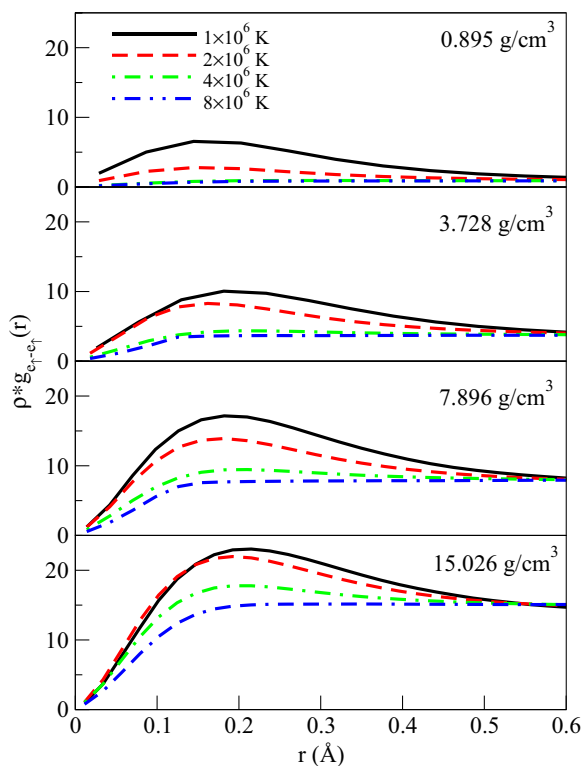


FIG. 9. (Color online) The electron-electron pair-correlation functions for electrons with parallel spins calculated with PIMC.
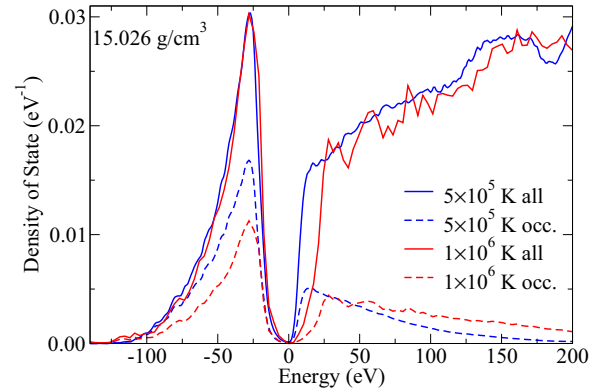


FIG. 10. (Color online) Electronic density of states of dense, fluid neon. The solid lines represent all available states while dashed lines show the occupied DOS. The curves are normalized such that the occupied DOS integrates to 1.

with the highest metallization pressure [37,38], followed by helium [39,40]. With DFT-MD simulations, it has been shown that the atomic disorder present in fluid helium reduces the metallization pressure significantly [41]. We therefore analyze the electronic density of states in our DFT-MD simulations of neon.

Figure 10 compares the total available DOSs and thermally occupied DOSs at a density of 15.0255 g cm$^{-3}$ and temperatures of $5 \times 10^5$ and $1 \times 10^6$ K. Results were obtained by averaging over at least 100 snapshots from equally spaced DFT-MD trajectories. The eigenvalues of each snapshot were aligned at their Fermi energy. To simplify Fig. 10, an additional shift is introduced to align the resulting gaps at zero.

The two occupied DOSs have large peaks near $-30$ eV reminiscent of the atomic $2s$ and $2p$ states, followed by a gap at the Fermi energy, which is then followed by a continuous spectrum of conducting states. For both temperatures, a large fraction of electrons are excited across the gap, which plays a role in the increase of pressure seen in Fig. 2 and in the increase of the compression ratio of Hugoniot curves discussed in the next section. Unlike hydrogen and helium, whose gaps close, turning them into metals [39,41–43], we do not find the gap for fluid neon closes for the even the most extreme conditions that we have studied here with DFT-MD.

## VI. SHOCK COMPRESSION

Dynamic shock compression experiments are the preferred laboratory experiments to probe the properties of materials at high pressure and temperature. Lasers [44], magnetic fields [45], and explosives [46] have been used to generate shock waves that reached megabar pressures. Density functional theory has been validated by experiments as an accurate tool for studying shock-compressed noble gases [47]. Under shock compression, the initial state of a material is characterized by internal energy, pressure, and volume $(E_0, P_0, V_0)$, which changes to a final state denoted by $(E, P, V)$. The conservation of mass, momentum, and energy yields the Hugoniot condition [48],

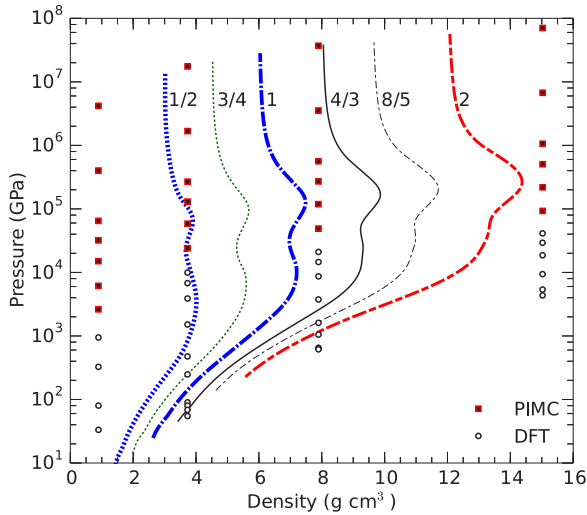$$H = (E - E_0) + \tfrac{1}{2}(P + P_0)(V - V_0) = 0. \quad (1)$$

FIG. 11. (Color online) Shock Hugoniot curve for different initial densities. The label on the curve specifies the ratio of the initial density to that of neon at 4 K, 1.5070 g cm$^{-3}$.



FIG. 12. (Color online) Hugoniot curves for different precompression ratios.

For one set of initial conditions, the shock Hugoniot curve refers to the collection of final states that can be obtained for different shock velocities. This curve can be predicted theoretically from an EOS table as given in Table I. For the initial state of the principal Hugoniot curve, we have chosen the density of solid neon at 4 K and ambient pressure, $\rho_0 = 1.5070$ g cm$^{-3}$ (Ref. [49]). We computed the corresponding internal energy with DFT calculations of a face-centered-cubic (fcc) solid. The resulting Hugoniot curve has been plotted in $T$-$P$ and $P$-$\rho$ spaces in Figs. 1 and 11, respectively.

Shock wave experiments have been performed in combination with diamond anvil cells in order to precompress the sample statically before a shock is launched. This technique allows one to increase the initial density and then reach much higher final densities. Thus density-temperature conditions much deeper in the interiors of planets can be reached [50]. We repeated our Hugoniot calculations for initial densities ranging from 1/2 to a 2-fold change of the ambient value, $\rho_0$. $P_0$ and $E_0$ were again derived from DFT calculations of an fcc solid since experimental [51–53] and theoretical [54] work consistently predict this crystal structure for solid neon.

Figure 11 shows the resulting family of Hugoniot curves. While starting from the ambient density had led to a maximal shock density of 7.202 g cm$^{-3}$, a 2-fold pre-compression to 13.6 GPa yields a much higher maximum shock density of 14.37 g cm$^{-3}$, as expected.

The shock compression behavior can best be analyzed by dividing the shock density by the initial density, which has been done for three representative Hugoniot curves in Fig. 12. In the high-temperature limit, all curves converge to a compression ratio of 4, which is the value of an ideal gas. However, compression ratios close to 4-fold may already be obtained at lower temperature where interaction effects are still important. In general, the shock compression ratio is controlled by the excitation of internal degrees of freedom, which increase the compression, and by interaction effects between particles that reduce it [55]. Consistent with our results for hydrogen and helium [12], we find that an increase in the initial density
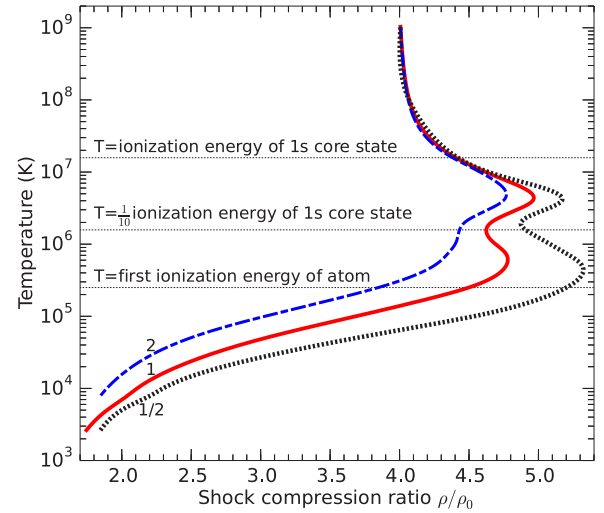
leads to a slight reduction in the shock compression ratio (Fig. 12) because particles interact more strongly at higher density.

The Hugoniot curves in Fig. 12 also exhibit two maxima if the shock densities are compared for different temperatures. The two compression maxima can be attributed to the ionization of electrons in the first and second shell. On the principal Hugoniot curve, the first maximum of $\rho/\rho_0 = 4.779$ occurs at temperature of $6.265 \times 10^5$ K (53.93 eV), which is above the first ionization energy of the neon atom, 21.56 eV. A second compression maximum of $\rho/\rho_0 = 4.968$ is found for a temperature of $4.355 \times 10^6$ K (375.3 eV). This maximum can be attributed to the ionization of the 1$s$ core states of the neon ions. From comparison, the ionization of the last electron requires an energy of 1360 eV. In the temperature interval near the compression maximum, (2–8) $\times 10^6$ K, we find a substantial reduction of the charge density around the nuclei, which we plotted in Fig. 6 confirming our ionization hypothesis.

Conditions where the 1$s$ state are partially or fully ionized are very difficult to study with DFT-MD simulations because one typically employs a pseudopotential with a frozen 1$s$ core to reach a level of efficiency that makes MD simulations with many particles possible in the first place. Thus, neon is the second material after helium [55] where it has been shown that PIMC simulations are necessary to determine the maximum compression along the principle Hugoniot curve.

## VII. CONCLUSIONS

In this work, we have combined PIMC with DFT-MD to construct a coherent EOS for neon over a large range of densities and temperatures. The two methods validate each other near temperatures of $1 \times 10^6$ K, where both methods are capable of producing results. This work presses the limits of our combined PIMC/DFT-MD approach for computing EOSs for WDM from first principles, where we employ only free-particle nodes in PIMC. Unlike hydrogen and helium, we do not find that the gap in the electronic density of states for neon closes for the most extreme conditions that

we studied here with DFT-MD. Our analysis of the pair-correlation functions describes how the structure of the plasma changes with temperature and density as atoms are ionized and electrons in the first and second shells become free. The ionization imprints a corresponding signature on the shock Hugoniot curves. We find that PIMC simulations are necessary to determine the state of the highest shock compression.

[1] M. Koenig *et al.*, Plasma Phys. Controlled Fusion **47**, B441 (2005).

[2] M. K. Matzen, Phys. Plasmas **12**, 055503 (2005).

[3] I. Cook, Nat. Mater. **5**, 77 (2006).

[4] R. Cauble, D. K. Bradley, P. M. Celliers, G. W. Collins, L. B. D. Siliva, and S. J. Moon, Contrib. Plasma Phys. **41**, 239 (2001).

[5] H. M. V. Horn, Science **252**, 384 (1991).

[6] G. Chabrier, F. Douchin, and A. Y. Potekhin, J. Phys. Condens. Matter **14**, 9133 (2002).

[7] J. J. Fortney, S. H. Glenzer, M. Koenig, B. Militzer, D. Saumon, and D. Valencia, Phys. Plasmas **16**, 041003 (2009).

[8] A. Bennuzzi-Mounaix, S. Mazevet, A. Ravasio, T. Vinci, A. Denoeud, M. Koenig, N. Amadou, E. Brambrink, F. Festa, A. Levy *et al.*, Phys. Scr., T **161**, 014060 (2014).

[9] J. M. Lattimer, Annu. Rev. Nucl. Part. Sci. **31**, 337 (1984).

[10] J. M. Dawson, Rev. Mod. Phys. **55**, 403 (1983).

[11] F. R. Graziani, V. S. Batista, L. X. Benedict, J. I. Castor, H. Chen, S. N. Chen, C. A. Fichtl, J. N. Glosli, P. E. Grabowski, A. T. Graf *et al.*, High Energy Density Phys. **8**, 105 (2012).

[12] B. Militzer, Phys. Rev. B **79**, 155105 (2009).

[13] K. P. Driver and B. Militzer, Phys. Rev. Lett. **108**, 115502 (2012).

[14] B. Militzer and D. M. Ceperley, Phys. Rev. E **63**, 066404 (2001).

[15] S. X. Hu, B. Militzer, V. N. Goncharov, and S. Skupsky, Phys. Rev. Lett. **104**, 235003 (2010).

[16] S. X. Hu, B. Militzer, V. N. Goncharov, and S. Skupsky, Phys. Rev. B **84**, 224109 (2011).

[17] L. X. Benedict, K. P. Driver, S. Hamel, B. Militzer, T. Qi, A. A. Correa, A. Saul, and E. Schwegler, Phys. Rev. B **89**, 224109 (2014).

[18] H. F. Wilson and B. Militzer, Phys. Rev. Lett. **104**, 121101 (2010).

[19] C. L. Chen, Phys. Rev. **135**, A627 (1964).

[20] R. Cauble, M. Blaha, and J. Davis, Phys. Rev. A **29**, 3280 (1984).

[21] J. Hughto, A. S. Schneider, C. J. Horowitz, and D. K. Berry, Phys. Rev. E **82**, 066401 (2010).

[22] D. M. Ceperley, Rev. Mod. Phys. **67**, 279 (1995).

[23] R. M. Martin, *Electronic Structure: Basic Theory and Practical Methods* (Cambridge University Press, UK, 2004).

[24] See Supplemental Material at http://link.aps.org/supplemental/10.1103/PhysRevB.91.045103 for time-step and finite-size convergence tests of the PIMC and DFT-MD calculations.

[25] D. M. Ceperley and B. J. Alder, Phys. Rev. Lett. **45**, 566 (1980).

[26] E. W. Brown, B. K. Clark, J. L. DuBois, and D. M. Ceperley, Phys. Rev. Lett. **110**, 146405 (2013).

[27] D. N. Mermin, Phys. Rev. **137**, A1441 (1965).

[28] F. Lambert, J. Clérouin, and S. Mazevet, Europhys. Lett. **75**, 681 (2006).

[29] G. Kresse and J. Furthmüller, Phys. Rev. B **54**, 11169 (1996).

[30] P. E. Blöchl, Phys. Rev. B **50**, 17953 (1994).

[31] J. P. Perdew, K. Burke, and M. Ernzerhof, Phys. Rev. Lett. **77**, 3865 (1996).

[32] P. Debye and E. Huckel, Phys. Z. **24**, 185 (1923).

[33] For OPIUM pseudopotential generation programs, see http://opium.sourceforge.net.

[34] M. Fuchs and M. Scheffler, Comput. Phys. Commun. **119**, 67 (1999).

[35] X. Gonze and C. Lee, Comput. Mater. Sci. **25**, 478 (2002).

[36] B. Militzer, J. Phys. A: Math. Theor. **42**, 214001 (2009).

[37] J. C. Boettger, Phys. Rev. B **33**, 6788 (1986).

[38] N. D. Drummond and R. J. Needs, Phys. Rev. B **73**, 024107 (2006).

[39] S. A. Khairallah and B. Militzer, Phys. Rev. Lett. **101**, 106407 (2008).

[40] B. Monserrat, N. D. Drummond, C. J. Pickard, and R. J. Needs, Phys. Rev. Lett. **112**, 055504 (2014).

[41] L. Stixrude and R. Jeanloz, Proc. Natl. Acad. Sci. U.S.A. **105**, 11071 (2008).

[42] P. Loubeyre, F. Occelli, and R. LeToullec, Nature (London) **416**, 613 (2002).

[43] R. E. Cohen, I. Naumov, and R. J. Hemley, Proc. Natl. Acad. Sci. U.S.A. **110**, 13757 (2013).

[44] J. Eggert, S. Brygoo, P. Loubeyre, R. S. McWilliams, P. M. Celliers, D. G. Hicks, T. R. Boehly, R. Jeanloz, and G. W. Collins, Phys. Rev. Lett. **100**, 124503 (2008).

[45] M. D. Knudson, D. L. Hanson, J. E. Bailey, C. A. Hall, and J. R. Asay, Phys. Rev. Lett. **90**, 035505 (2003).

[46] V. E. Fortov, R. I. Ilkaev, V. A. Arinin, V. V. Burtzev, V. A. Golubev, I. L. Iosilevskiy, V. V. Khrustalev, A. L. Mikhailov, M. A. Mochalov, V. Y. Ternovoi *et al.*, Phys. Rev. Lett. **99**, 185001 (2007).

[47] S. Root, R. J. Magyar, J. H. Carpenter, D. L. Hanson, and T. R. Mattsson, Phys. Rev. Lett. **105**, 085501 (2010).

[48] Y. B. Zeldovich and Y. P. Raizer, *Elements of Gasdynamics and the Classical Theory of Shock Waves* (Academic Press, New York, 1968).

[49] D. N. Batchelder, D. L. Losee, and R. O. Simmons, Phys. Rev. **162**, 767 (1967).

[50] B. Militzer and W. B. Hubbard, AIP Conf. Proc. **955**, 1395 (2007).

[51] R. J. Hemley, C. S. Zha, A. P. Jephcoat, H. K. Mao, L. W. Finger, and D. E. Cox, Phys. Rev. B **39**, 11820 (1989).

[52] A. Dewaele, F. Datchi, P. Loubeyre, and M. Mezouar, Phys. Rev. B **77**, 094106 (2008).

[53] K. Takemura, T. Watanuki, K. Ohwada, A. Machida, A. Ohmura, and K. Aoki, J. Phys.: Conf. Ser. **215**, 012017 (2010).

[54] Y.-G. He, X.-Z. Tang, and Y.-K. Pu, Physica B **405**, 4335 (2010).

[55] B. Militzer, Phys. Rev. Lett. **97**, 175501 (2006).